



Film thickness measurements for annular flow in minichannels: Description of the optical technique and experimental results

A. Donniacuo ^a, R. Charnay ^b, R. Mastrullo ^a, A.W. Mauro ^a, R. Revellin ^{b,*}

^a University of Naples Federico II, Department of Industrial Engineering, P.le Tecchio 80, 80125 Naples, Italy

^b Université de Lyon, INSA-Lyon, CETHIL UMR5008, F-69621 Villeurbanne, France

ARTICLE INFO

Article history:

Received 27 January 2015

Received in revised form 7 July 2015

Accepted 7 July 2015

Available online 29 July 2015

Keywords:

Minichannel

Annular flow

Film thickness

Optical measurement technique

Stratification

ABSTRACT

An optical method is developed in order to measure the top and bottom liquid film thicknesses during evaporative annular flow in a horizontal minichannel. This method is based on the detection of liquid-vapor and liquid-solid interfaces. For each flow condition, about 4000 frames (corresponding to an observation time of 2 s) are recorded with a high-speed camera. Thus, these frames are processed with an image processing algorithm to obtain the average liquid film measurement. Three different configurations of the camera are tested. The chosen solution ensures a good reliability and accuracy of film measurements. The view section is a 2.95 mm glass circular channel and the working fluid is R-245fa. The tests are performed in annular flow, for different vapor qualities. A test facility allows reaching the desired conditions of the flow at the inlet of the test section. The examined saturation temperatures are 40, 60, 80 and 100 °C, whereas the mass velocities are 300 and 400 kg/m² s. A parameter of eccentricity is introduced to characterize the stratification effect. The influence of the saturation temperature, mass velocity and vapor quality is physically discussed through the Froude and Bond numbers. Finally, by using the top and bottom liquid film measurements, the cross-sectional void fraction is estimated.

© 2015 Elsevier Inc. All rights reserved.

1. Introduction

In industrial processes, power plants and road transport industry new methods and technologies have been studied to reduce fuel consumption and consequently CO₂ emissions by energy conversion from low temperature waste heat recovery. Among the proposed methods, the Organic Rankine Cycle (ORC) is one of the most promising. In facts, ORC's cycles are basic systems for energy conversion and they may have a good matching with the thermal source with an appropriate choice of the operating fluid. Studies available in literature (see for example [1,2]) discussed several issues about the technology development and the selection of the working fluid depending of the application. As pointed out by Cataldo et al. in [3] in the range of source temperatures around 100–150 °C the optimal pair evaporating/condensing temperature is a feature of the working fluid. Most promising working fluids are natural ones (even if toxicity/flammability problems raise with their adoption) or hydrofluorocarbon mixtures. The latter ones have the advantage to be currently used in the refrigeration sector and the related materials and technologies need small adaptation in terms of chemical compatibility and age testing. In addition,

technology for heat exchanger development is available. Research studies have been carried out to furnish the technical support for appropriate design of components. Concerning the heat exchanger design, the priority has been to have new insights into the two-phase heat transfer at evaporating temperatures higher than those commonly used in the refrigerating sector and at higher reduced pressure (up to 0.8 for some HFC mixtures). Charnay et al. [4] showed that there are almost no data at high saturation temperatures. In their work [4] they demonstrated that the method by Cioncolini and Thome [5] is the best one for R-245fa fluids for reduced pressures up to 0.3. Del Col [6] studied flow boiling of halogenated refrigerants up to a reduced pressure of 0.50 assessing predictive methods and proposed a new correlation. Grauso et al. [7] demonstrated how at medium reduced pressure (up to 0.69) the predictive methods for flow boiling in macro-channels have often a weak accuracy in heat transfer calculations due to increased liquid thickness at the wall and, for horizontal flows, stratification of the liquid at the bottom.

For ORC evaporators the concurrent increase of the saturation temperature and thus of the reduced pressure makes the stratification effects during horizontal annular flows of primary importance. The non-uniformity in the annular film on the heat transfer process has been investigated by Mauro et al. [8], which stated that local measurements around the perimeter of horizontal tubes could

* Corresponding author.

E-mail address: remi.revellin@insa-lyon.fr (R. Revellin).

Nomenclature

| | |
|------|--|
| A | cross sectional area (m^2) |
| Bd | Bond number (-) |
| d | view section diameter (m) |
| D | detected diameter (pixel) |
| EF | enlargement factor (-) |
| Fr | Froude number (-) |
| G | mass velocity ($\text{kg}/\text{m}^2 \text{s}$) |
| g | gravitational acceleration (m/s^2) |
| MAE | mean absolute error (%) |
| MRE | mean relative error (%) |
| n | refractive index (-) |
| R | view section radius (m) |
| r | vapor core radius (m) |
| Sc | scale conversion (pixel/mm) |
| T | temperature (K) |
| x | vapor quality (-) |

| <i>Greek symbols</i> | |
|----------------------|------------------------------------|
| δ | film thickness (m) |
| ε | void fraction (-) |
| θ | angle (rad) |
| ρ | density (kg/m^3) |
| σ | surface tension (N/m) |

Subscripts

| | |
|-----|------------|
| bot | bottom |
| in | inner |
| liq | liquid |
| out | outer |
| sat | saturation |
| top | top |
| vap | vapor |

show a significant variation, up to 25–30% in heat transfer from top to bottom. In addition, during the process of evaporation in horizontal tubes, the top of the tube is more quickly dried out due to the thinner thickness of the liquid film. Different authors observed this phenomenon by assessing a drastic drop of heat transfer coefficient at the top of the tube (Mori et al. [9], Wojtan et al. [10], Mastrullo et al. [11], and Charnay et al. [12]). Therefore, it is important to have experimental data regarding liquid film thickness around the tube perimeter to calibrate appropriately heat transfer models and predict the transition to critical conditions (as the dry-out).

In literature, several studies are available concerning the circumferential liquid film measurements for horizontal annular flow. Luninski et al. [13], performed measurements for air–water mixtures, with pipe diameters ranging from 8.15 to 12.5 mm. They measured the film thickness for different positions around the tube periphery. Other experiments were performed by Lauriat and Hanratty [14], Fukano and Ousaka [15], Hurlburt and Newell [16], Shedd and Newell [17]. The cited papers refer to measurements for air–water flows at room temperature. The variation of the gas to liquid density ratio, viscosity ratio and surface tension are correspondingly very limited. Being difficult to have reliable extrapolate predictions using predictive methods far from their calibration range, additional measurements for refrigerants under operating conditions close to the real operation are needed [18].

In the present study, a new optical technique for the measurement of top and bottom film thicknesses during a two-phase annular flow in a horizontal minichannel is introduced. Then experimental data of the liquid thicknesses at the top and bottom of the tube are presented and commented for a minichannel with an internal diameter of 2.95 mm, for evaporating temperatures between 40 and 100 °C and mass fluxes between 300 and 400 $\text{kg}/\text{m}^2 \text{s}$.

2. Experimental setup

An experimental test facility, described by Charnay et al. [19], allows reaching the desired conditions of the flow at the inlet of the test section, i.e. mass flow rate, inlet subcooling and saturation pressure.

The test bench, presented in Fig. 1, has three methods for controlling the flow through the heat transfer and flow visualization test sections: either by controlling the rotational velocity of the

pump, or by activating the by-pass valve, or by activating a microvalve placed at the inlet of the test section. Liquid refrigerant is moved by a gear pump and passes through a filter/dryer, a Coriolis-type flowmeter, a microvalve, the test section and a condenser, which is a plate heat exchanger. A controlled-temperature reservoir allows fixing the saturation pressure in the loop.

The test section, shown in Fig. 2, consists in three parts:

- A 2000 mm spirally shaped stainless steel tube (preheater). The inner and outer diameters are 3.00 mm and 5.99 mm respectively.
- A 185 mm stainless steel horizontal tube (evaporator). The inner and outer diameters are the same of the preheater.
- A 200 mm glass visualization tube. The inner and outer diameters (d_{in} and d_{out}) are 2.95 mm and 5.95 mm.

The preheater ensures the control of the vapor quality at the heat transfer test section inlet by two copper clamps connected electrically to a power supply. The evaporator is heated by the same method. The vapor quality at the inlet of the flow visualization section is evaluated at the outlet of the evaporator, with the hypotheses of negligible heat loss and pressure drop. By keeping the same assumptions, the saturation pressure is measured at the outlet of the evaporator. Before running boiling experiments, single-phase tests were performed with R-245fa to estimate the heat losses in the preheater and the evaporator. The heat losses rate is around 7% and 3% for the preheater and the evaporator respectively. Thus, the energy balance for both is validated. A Coriolis-type flowmeter was used to measure the mass flow rate with an accuracy of $\pm 0.2\%$. The Joule heating power was obtained by measuring the DC voltage and the DC current by a SORENSEN acquisition system. The accuracy is $\pm 90 \text{ mV}$ and $\pm 100 \text{ mA}$ for the preheater and $\pm 12 \text{ mV}$ and $\pm 1400 \text{ mA}$ for the evaporator. The absolute pressure transducers are accurate to $\pm 70 \text{ mbar}$. The differential pressure transducer measures the pressure drop along the evaporator with an accuracy of $\pm 2 \text{ mbar}$. Thermocouples are accurate to $\pm 0.25 \text{ }^\circ\text{C}$. The vapor quality at the outlet of the test section is determined by using the refrigerant properties calculation software RefProp once the pressure (directly measured with an absolute pressure transducer) and the enthalpy (determined by an energy balance from the inlet of the pre-heater to the outlet of the evaporator) are known. The maximum error on the vapor quality is ± 0.03 .

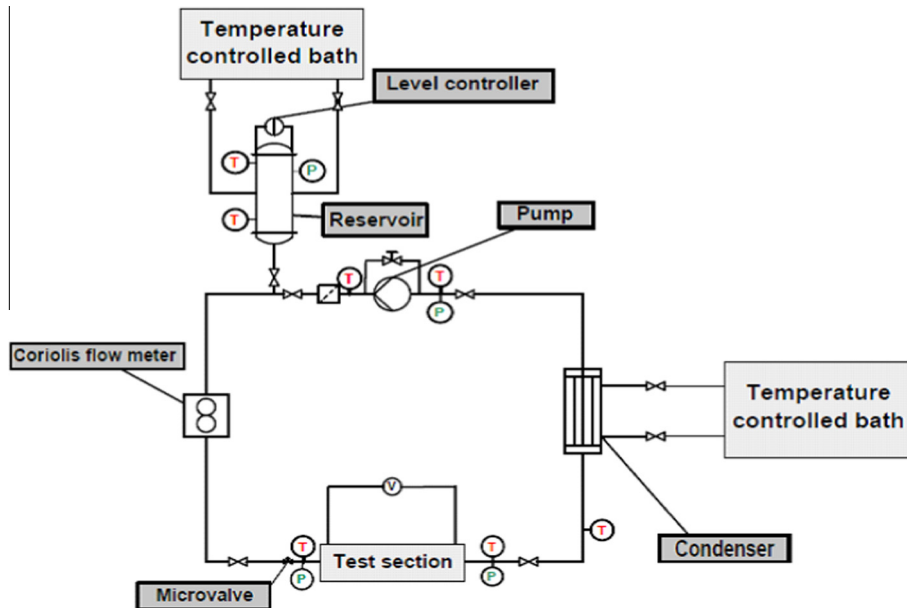


Fig. 1. Schematic of test facility, Charnay et al. [19].

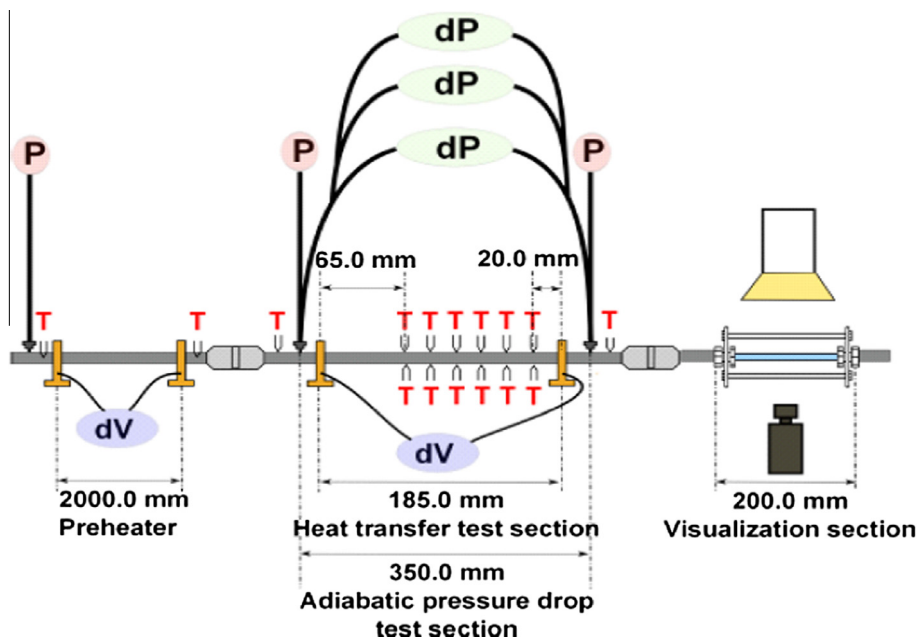


Fig. 2. Schematic of test section, Charnay et al. [19].

3. Optical measurement technique

In the literature, different studies for the liquid film measurement were performed. Most of studies are relative to adiabatic two-phase mixtures. A review of Tibiriçá et al. [20] summarizes the main measurement techniques for macro-scale and micro-scale flows. These techniques are mainly based on acoustic, electrical and optical methods. Among the optical techniques, Hurburt and Newell [16] developed an optical technique based on the total reflection of light. This technique was lately improved by Shedd and Newell [17]. Takamasa and Hazuku [21] and Takamasa and Kobayashi [22] developed a laser focus displacement technique in order to precisely measure dynamic film thickness. Ong and Thome [23], based on the detection of liquid–vapor

and liquid–solid interfaces, developed an image processing method to determine the film thickness in terms of number of image pixel.

In this paper, an optical measurement technique was developed to measure the liquid film thickness. The instruments used are a high-speed image acquisition system and an image processing program written under Matlab environment. A high-speed camera system (Photron Fastcam SA3 120KM2) allows the flow visualization by recording image sequences. The light system used for the visualization is provided through an adjustable light behind the visualization glass tube. The optical arrangement is a backlit imaging arrangement, resulting in a light gradient at the liquid–vapor interface due to shadowgraph effect. Concerning the light source, a 400 W Dedolight HMI lamp is chosen. This lamp presents a collimating system. Furthermore, the half angular spread of the beam is

set to the minimum value (2.4°) to minimize errors due to beam spread. Therefore, it is assumed the hypothesis of the horizontal ray of light tangent to the liquid–vapor interface.

3.1. Optimal high-speed camera configuration

Three different configurations of the camera were compared in order to choose the most appropriate for the film measurement. A schematic of the first configuration is given in Fig. 3 and an example of recorded frame, which size is 1024×128 pixels, is shown in Fig. 4a.

Nevertheless, this configuration cannot provide accurate details on the liquid film thickness. Indeed, the ratio pixel/mm is quite low, close to 10. In order to obtain detailed information of the local liquid film thickness, a bellows was mounted between the lens and the camera body and the camera is focused on a little part of the view section. This is the second camera configuration. With this arrangement, the size of the images is 1024×1024 pixels and the ratio pixel/mm is about 160. An example of recorded frame is shown in Fig. 4b. The third configuration consists of a microscope

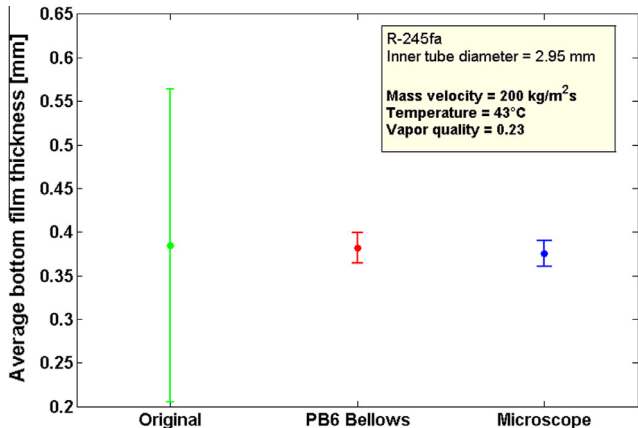


Fig. 5. Comparing bottom film thicknesses, obtained with the three configurations of the high-speed camera. The conditions of the flow are mass velocity of $200 \text{ kg/m}^2 \text{ s}$, saturation temperature of 43°C and vapor quality of 0.23.

Table 1
Optical measurement conditions.

| Parameter | Value | Units |
|------------------|--------------------|---------|
| Frame rate | 2000 | Frame/s |
| Shutter time | $1/402,200$ | s |
| Acquisition time | 2 | s |
| Frame size | 1024×1024 | pixel |
| Greyscale value | 0–255 | |

coupled with the camera. The size of the images is 1024×1024 pixels and the ratio pixel/mm rises to 470 pixel/mm. An example of frame is shown in Fig. 4c.

In order to choose the best configuration for further analyses, a measurement of film thicknesses was performed for the three camera configurations, during the same flow conditions. In Fig. 5 the mean values of the bottom film measurements, together with the error bar is shown. The configuration 1 is not reliable, because of the low ratio pixel/mm. The configuration 2 (bellows) gives quite similar results compared to the configuration 3 (microscope). The latter presents the lower uncertainty. Nevertheless, this solution

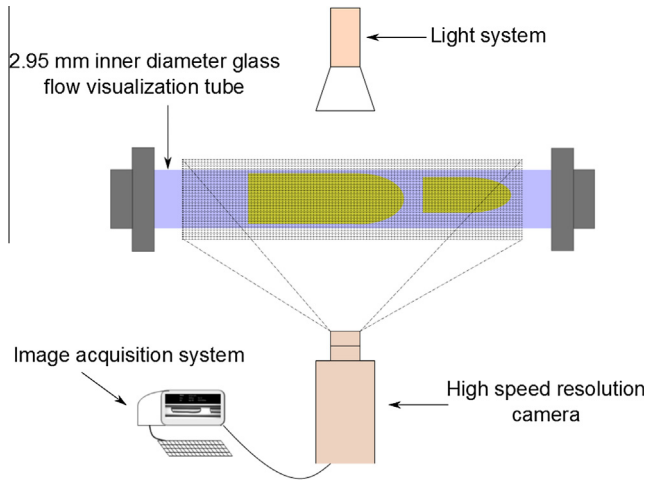


Fig. 3. Schematic of image acquisition system: first configuration of the camera.

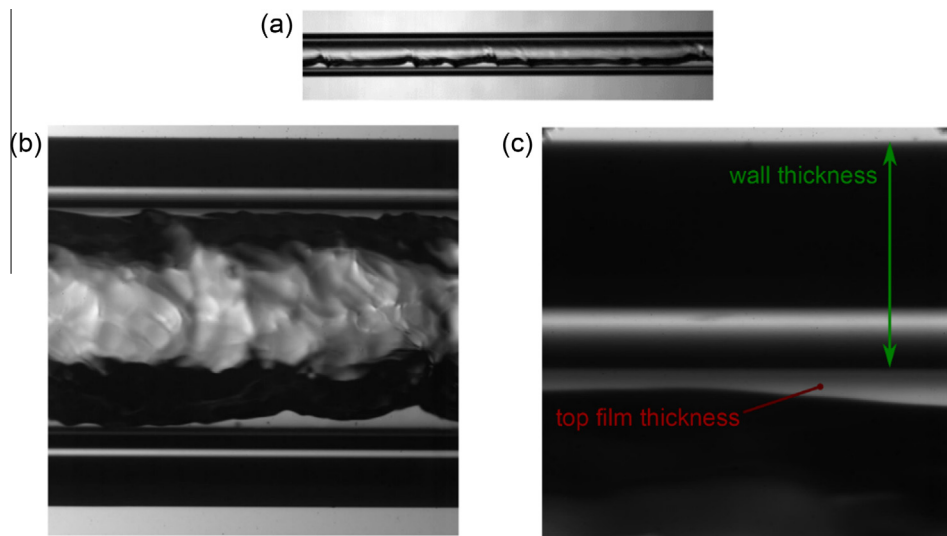


Fig. 4. Two-phase flow in the view section recorded with the three different camera configurations: (a) original camera configuration: 1024×128 pixels – 10 pixel/mm; (b) bellows mounted on the camera: 1024×1024 pixels – 160 pixel/mm; (c) microscope coupled with the camera: 1024×1024 pixels – 470 pixel/mm.

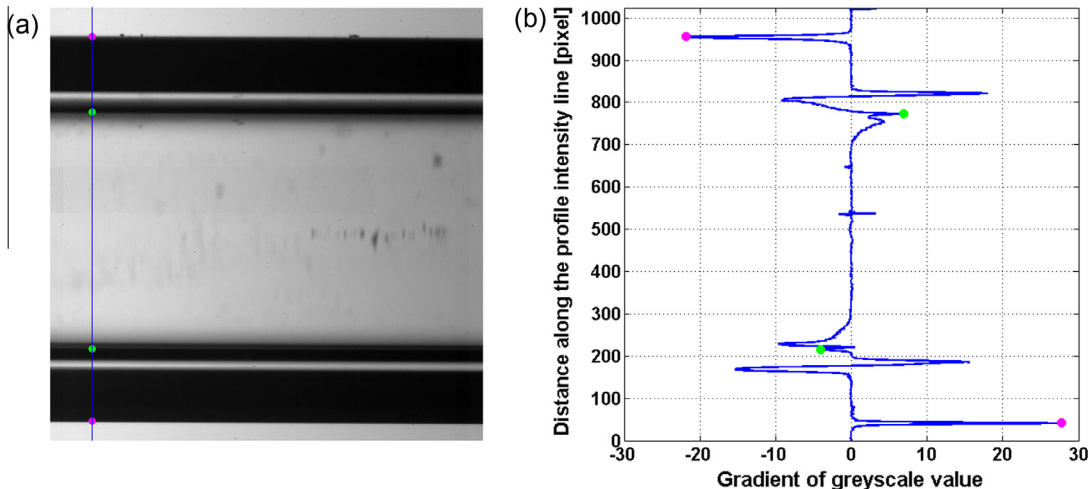


Fig. 6. (a) Picture of a liquid single-phase flow with detection of the inner and outer wall boundaries; (b) gradient of the intensity profile line and peaks detection at the inner and outer wall boundaries.

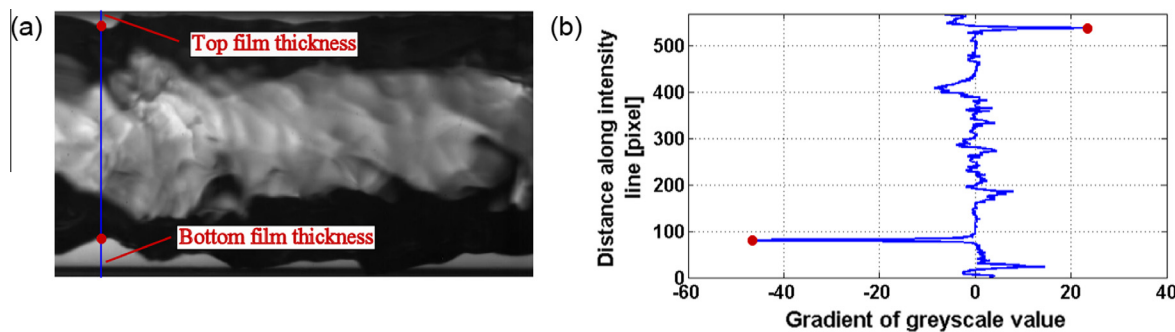


Fig. 7. (a) Picture of a two-phase flow cut at the inner wall boundaries, with detection of liquid–vapor interfaces; (b) gradient of the intensity profile line and local peaks detection, corresponding to liquid–vapor interfaces.

Table 2
Refraction index of liquid R-245fa, n_{liq} , for different temperatures (Schmidt et al. [26]).

| T (K) | 299 | 333 | 353.3 | 373.4 |
|----------------------|--------|--------|--------|--------|
| n_{liq} (-) | 1.2553 | 1.2353 | 1.2217 | 1.2080 |

has some limits. In fact, the recorded frames show just a part of the cross section (see Fig. 4c). Therefore, information on the flow pattern are lost and it is not possible to record at the same time both top and bottom film thicknesses.

For these reasons, the configuration 2 (bellows) was chosen for the film measurements. Table 1 summarizes the main parameters of the image acquisition. The recording speed of 2000 frames/s is a good trade-off between file size and image quality for the required

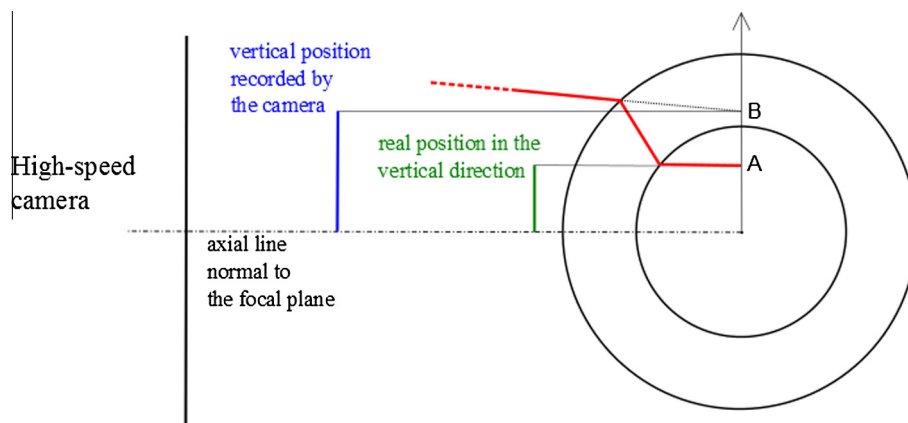


Fig. 8. Schematic of the refraction effects inside the tube. A is the real position of a point inside the tube in the vertical direction; B is the vertical position of the same point viewed by the camera.

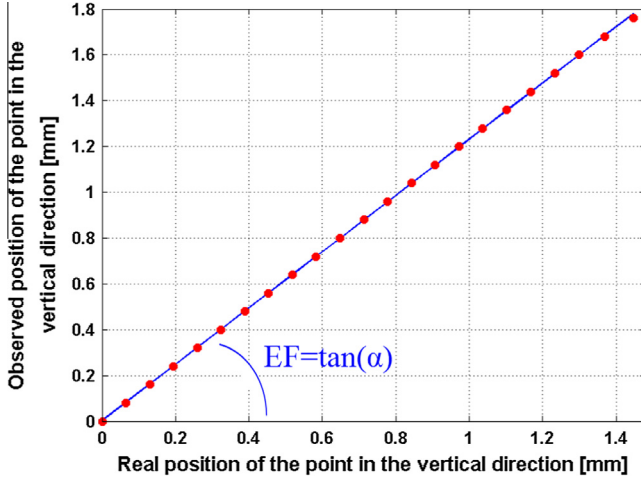


Fig. 9. Refraction effects inside the tube. The x-axis indicates the real position of a point inside the tube in the vertical direction; the y-axis shows the vertical position of the same point viewed by the camera. The slope of the linear approximation is the enlargement factor, EF .

target. For each condition of the flow, three videos of 0.68 s are performed, resulting in 4089 frames. The size of the image is 1024×1024 pixels, each pixel has a grayscale value ranging from 0 to 255.

3.2. Image processing method

This section is related to the second configuration of the camera as showed before. To measure the liquid film thickness, the liquid-vapor interface and liquid-wall boundaries are detected by the corresponding local gradient peaks of light intensity in the vertical direction. The first step of the image processing algorithm is the detection of the inner and outer wall boundaries for a liquid single-phase flow (see Fig. 6a). This is achieved by setting a profile line is at a fixed abscissa and by measuring the intensity values of each pixel along this profile. It is possible to detect the boundaries by finding the local peaks of the gradient of the intensity function (see Fig. 6b). A great number of frames are analysed in order to have a more reliable result. It is underlined that profile line was placed as close as possible to the entrance of the glass tube (1 cm). Indeed, the vapor quality entering the flow visualization section was determined at the outlet of the evaporator. However, it was verified that vapor quality variation was negligible.

After the boundaries detection in single-phase flow, the frames are cut at the inner wall boundaries and the top and bottom liquid-vapor interfaces are detected, as shown in Fig. 7a. The detection is

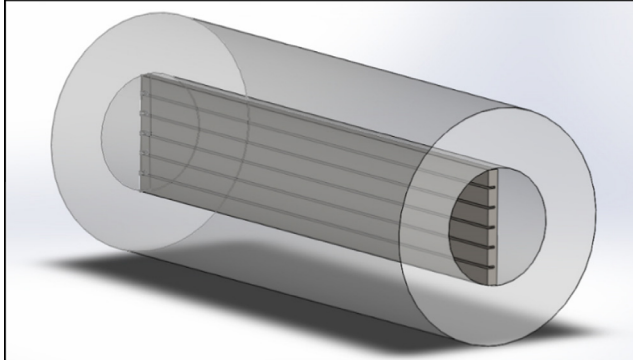


Fig. 10. Schematic of the target used for the validation of the optical model.

performed thanks to the shadowgraph effect resulting in a local gradient peak of light intensity (see Fig. 7b). At this point, the film thickness in terms of pixel is known.

The scale conversion (Sc (pixel/mm)) is provided by the ratio between the number of pixels required to display the cross-section of the tube (D_{out}) and the value of the outer diameter (d_{out}):

$$Sc = \frac{D_{out}}{d_{out}} \quad (1)$$

The uncertainties on D_{out} and d_{out} are ± 2 pixels and ± 0.03 mm respectively. The scale conversion is 160 pixel/mm, with an uncertainty of ± 0.4 pixel/mm.

3.3. Correction of refraction effects

Since the direct measurement suffers of the refraction effects through the glass of the tube, a correction factor was introduced. Kawahara et al. [24] performed an optical investigation of two-phase flow in a horizontal microchannel. They observed a magnification of the internal diameter of 50% due to the refraction

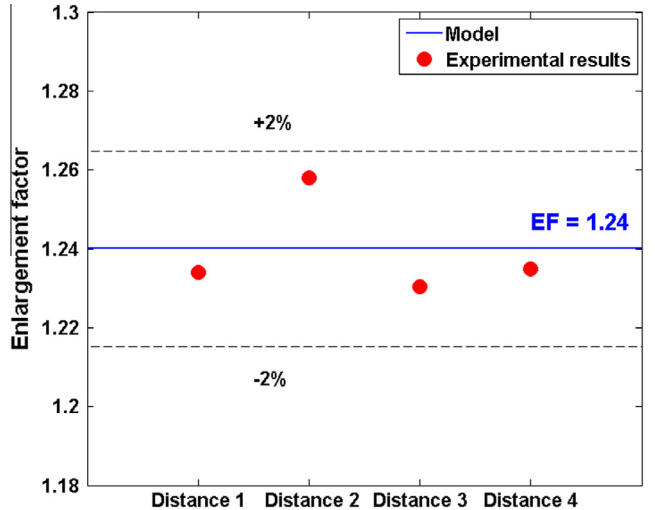


Fig. 11. Comparison of the experimental enlargement factor with the value provided by the model.

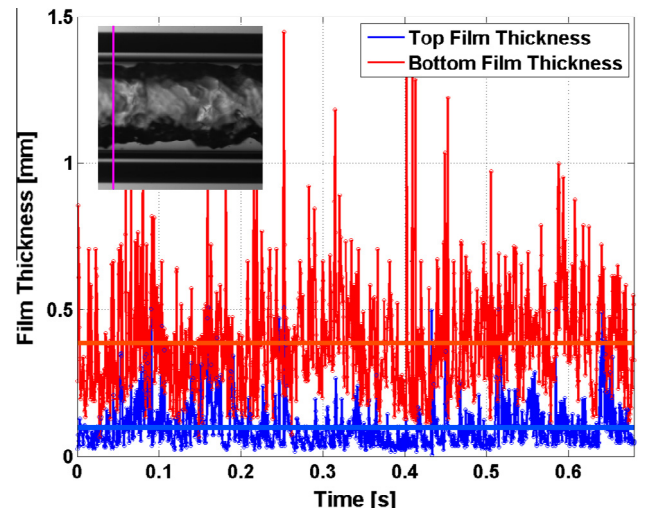
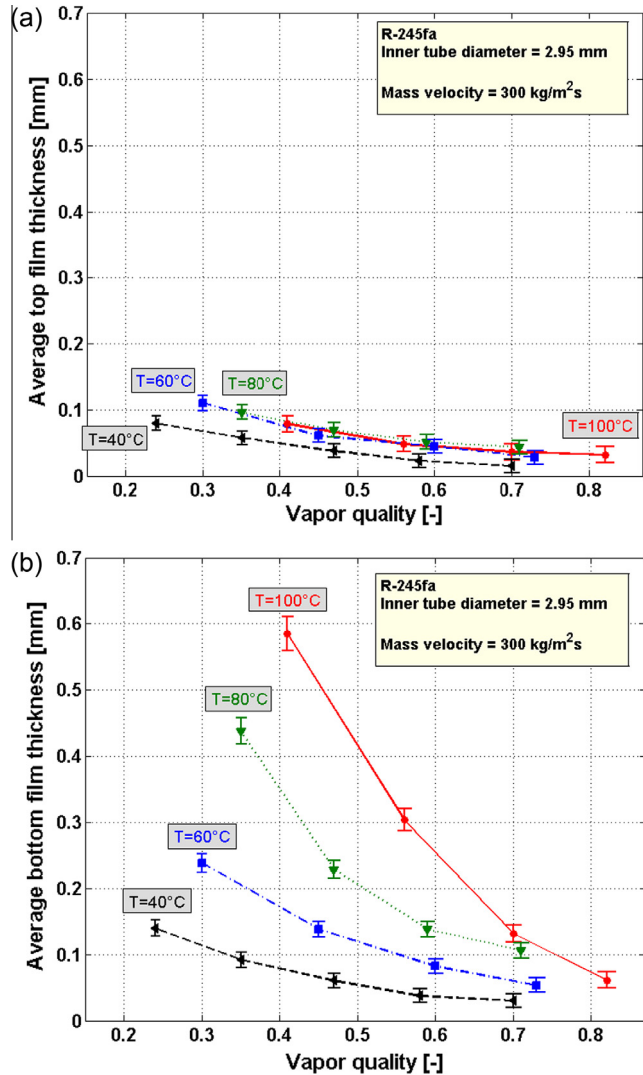


Fig. 12. Local and average film thicknesses a saturation temperature of 80 °C, mass velocity of $300 \text{ kg/m}^2 \text{ s}$ and vapor quality of 0.35.

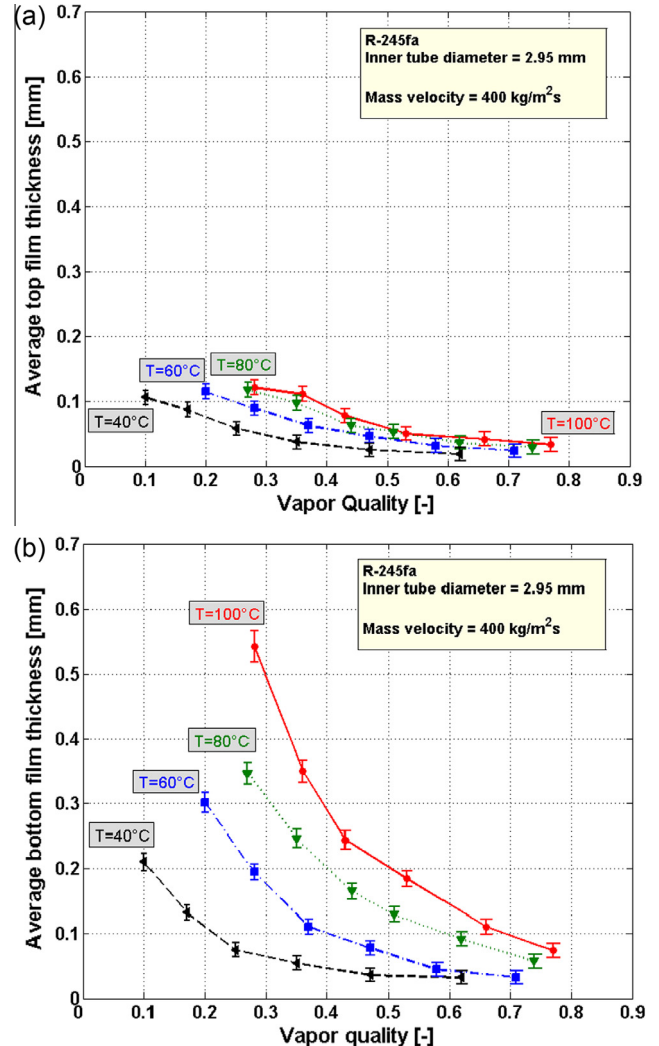
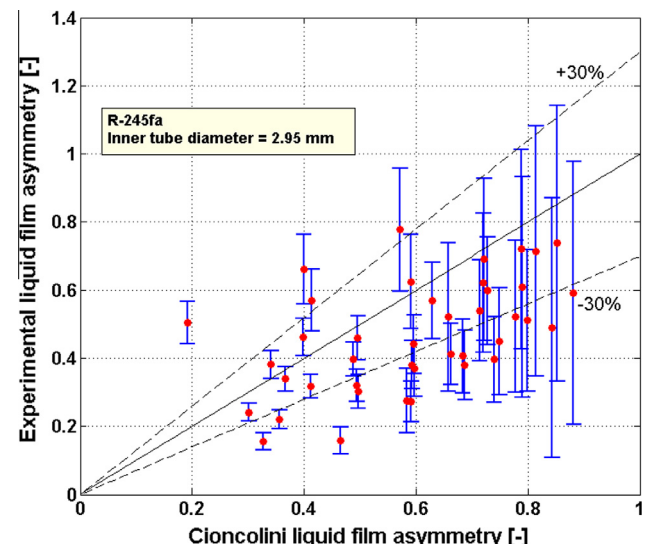
Table 3

Experimental conditions for liquid film measurements with refrigerant R-245fa.

| Parameter | Range |
|---------------------------|----------|
| d_{in} (mm) | 2.95 |
| d_{out} (mm) | 5.95 |
| T_{sat} (°C) | 40–100 |
| G (kg/m ² s) | 300–400 |
| x (-) | 0.1–0.82 |

**Fig. 13.** Top (a) and bottom (b) film thickness measurements, for a mass velocity of 300 kg/m²s and saturation temperatures of 40, 60, 80 and 100 °C.

effects. The optical distortion has an effect only in the radial direction without affecting the axial view of the tube. They also pointed out that the measured liquid film thickness is significantly greater than the real film thickness due to the optical distortion effect, so quantitative analyses require an appropriate correction. Concerning two-phase flows in micro-tubes, Fu et al. [25] performed both a theoretical and experimental approach for the quantification of the image deformation. They developed a simple optical model. According to this model, the image enlargement compared to the real situation depends on two factors: the different refractive indexes of the glass tube and the fluid and the geometrical configuration of the test section. This model was used to evaluate the distortion of the top and bottom liquid film thickness

**Fig. 14.** Top (a) and bottom (b) film thickness measurements, for a mass velocity of 400 kg/m²s and saturation temperatures of 40, 60, 80 and 100 °C.**Fig. 15.** Comparison between experimental film thickness ratios with the values given by Cioncolini and Thome correlation.

in our configuration. Therefore, the refractive index of liquid R-245fa is needed, that is a function of the temperature, as shown by Schmidt et al. [26] (see Table 2). Here an averaged value is considered.

Appling the formulas of the model, for each point inside the horizontal tube, the apparent position viewed by the camera is known. A schematic is shown in Fig. 8. The linear approximation

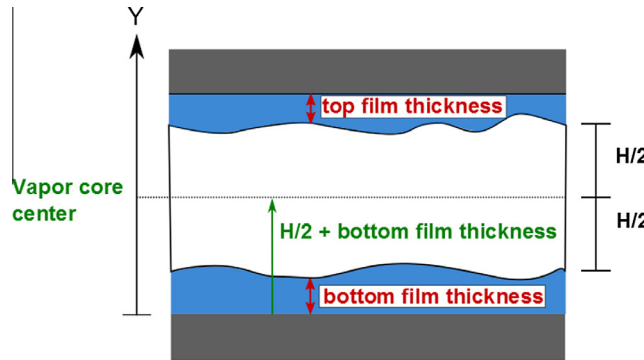


Fig. 16. Position of the vapor core center in vertical direction.

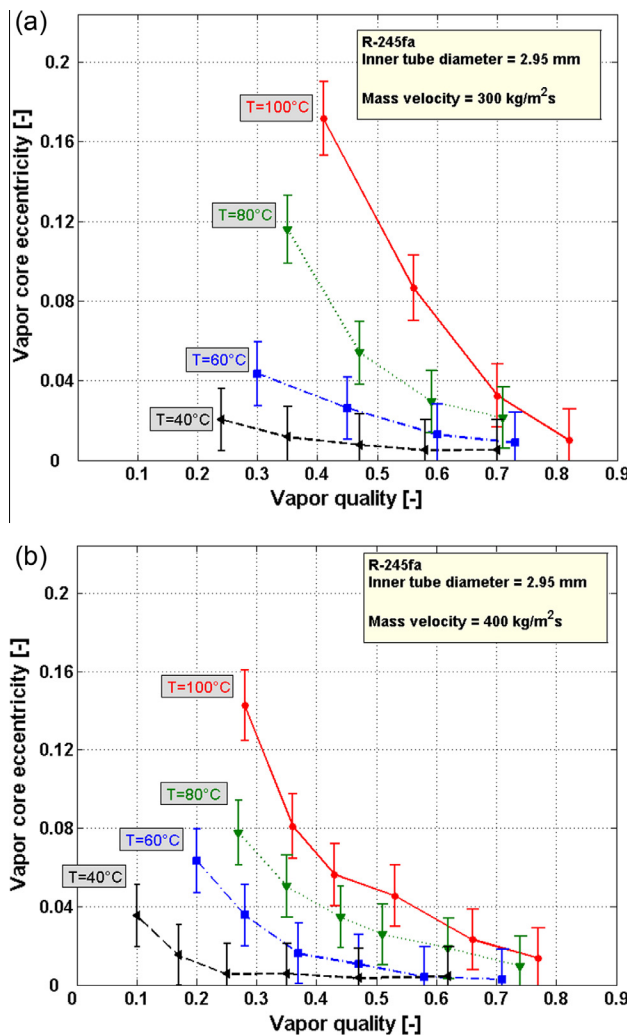


Fig. 17. Eccentricity of the vapor core for $G = 300$ (a) and 400 (b) $\text{kg}/\text{m}^2 \text{s}$, with $T_{\text{sat}} = 40, 60, 80$ and 100°C .

of these points shows a low mean square error (see Fig. 9). For this reason, a uniform enlargement in the vertical direction was assumed. The slope of the regression line is the enlargement factor, the value of which is 1.24.

The next step was to perform some experimental tests to validate the optical model. A metallic target was placed inside the glass tube. This target has a height equal to the internal diameter of the pipe and a negligible width compared to its height. There are five grooves every 0.5 mm in the direction of the tube diameter, as shown in Fig. 10. The distances between adjacent grooves were measured with a scanning electron microscope. Only liquid phase flowed inside the view section, because the purpose was to evaluate refraction effects for the liquid R-245fa.

Through the image processing, the distance in pixels between two adjacent grooves was calculated. The apparent distance (mm) was evaluated through the scale conversion factor (Sc (pixel/mm)). Hence, by knowing the real distance values, the enlargement for each distance was known. The comparison with the model provides good results (see Fig. 11). Therefore, a uniform enlargement factor, EF , was assumed, which value is 1.240 ± 0.047 .

Consequently, the real value of the liquid film thickness for each picture was calculated as follows:

$$\text{Real film thickness (mm)} = \frac{\text{Apparent film thickness (pixel)}}{EF (-) \cdot Sc (\text{pixel}/\text{mm})} \quad (2)$$

The uncertainty on the apparent film thickness is ± 2 pixels. At each operating condition, the top and bottom liquid film thickness were calculated as the average value from 4069 recorded frames, as shown in Fig. 12.

For each measurement was also calculated the error bar, taking into account several sources of uncertainty: inner and outer diameter dimensions; variation of liquid R-245fa refractive index with the temperature; limitations of image resolution, due to finite pixel dimensions. The combined uncertainty for film thickness measurement was evaluated, according to the method proposed by Taylor [27], as:

δ Real film thickness

$$= \sqrt{\left(\frac{1}{EF \cdot Sc} \cdot \delta \text{ Apparent film thickness}\right)^2 + \left(\frac{\text{Apparent film thickness} \cdot \delta EF}{-Sc \cdot EF^2}\right)^2 + \left(\frac{\text{Apparent film thickness} \cdot \delta Sc}{-EF \cdot Sc^2}\right)^2} \quad (3)$$

For the operating conditions presented in this paper, the mean uncertainty of film measurement is about 20%.

4. Experimental results

4.1. Experimental conditions

The experiments were performed in annular flow for mass velocities, G , equal to 300 and 400 $\text{kg}/\text{m}^2 \text{s}$ and saturation temperatures, T_{sat} , of 40, 60, 80 and 100 $^\circ\text{C}$. For each operating condition, different vapor qualities, x , were analysed, in a range depending on the mass velocity and the saturation temperature. The experimental condition are summed up in Table 3.

4.2. Film thickness measurements

As shown in Figs. 13b and 14b, for both $G = 300$ and $400 \text{ kg}/\text{m}^2 \text{s}$, the bottom film thickness clearly increases with the saturation temperature. Concerning the top film thickness (see Figs 13a and 14a), at low T_{sat} , there is no variation. This means that when increasing the temperature, the vapor core occupies a smaller

percentage of the section. This result can be explained by a greater density ratio $\rho_{\text{vap}}/\rho_{\text{liq}}$.

In literature, there are not available method to predict liquid film thickness for evaporative two-phase flow in small channels. The actual methods usually refers to film thickness concerning air–water flows in macrochannels. However, in Fig. 15 was performed a comparison with Cioncolini and Thome [18] correlation. The authors correlates the film thickness ratio to the Froude number through the following correlation:

$$\frac{\delta_{\text{top}}}{\delta_{\text{bot}}} = \frac{0.0789 \text{Fr}^{1.9}}{1 + 0.0789 \text{Fr}^{1.9}} \quad (4)$$

The parameters of the latter function were determined from experimental data using a nonlinear regression technique of experimental data, most referring to air–water flows in macrochannels. The comparison with experimental data is shown in Fig. 15.

4.3. Stratification effect: eccentricity of the vapor core

In the literature, the stratification for adiabatic two-phase flows is often evaluated by using the ratio $\delta_{\text{top}}/\delta_{\text{bot}}$ of the liquid film thickness at the tube top, δ_{top} , to the liquid film thickness at the

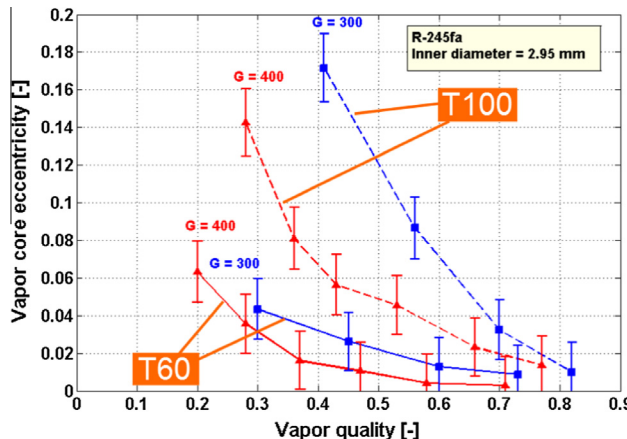


Fig. 18. Influence of mass velocity on stratification: eccentricity at $T_{\text{sat}} = 60$ and 100°C for both $G = 300$ and $400 \text{ kg/m}^2 \text{ s}$.

tube bottom, δ_{bot} . In the present study, the eccentricity of the vapor core is introduced to characterize the stratification effect. This parameter is defined as:

$$\text{eccentricity} =$$

$$\frac{\text{Position of vapor core center from the bottom-internal radius}}{\text{internal radius}} \quad (5)$$

According to the schematic given in Fig. 16, it is possible to verify that the position of the vapor core center is the sum of $H/2$ and the bottom film thickness.

When eccentricity is 0 there is no stratification since the bottom and top thickness are equal. On the contrary, the ideal limit for the maximum stratification is 1 which occurs when all the liquid is at the bottom and the bottom thickness tends to the internal diameter.

Fig. 17 reports the eccentricity for both mass fluxes, $G = 300$ and $400 \text{ kg/m}^2 \text{ s}$, and the whole set of saturation temperatures. Independently of the mass flux, the trend with the vapor quality is the same: the stratification increases with T_{sat} and decreases with x . In particular, for $T_{\text{sat}} = 40$ and 60°C the value of the eccentricity is very small, even for low vapor quality. On the contrary, for a saturation temperature of 100°C the eccentricity is relevant. In Fig. 18 the influence of the mass velocity for $T_{\text{sat}} = 60$ and 100°C is reported. The eccentricity is higher at lower mass fluxes, for fixed saturation temperature and vapor quality.

4.4. Dimensionless analysis

In order to relate the trends of the eccentricity to the forces acting at the liquid–vapor interface and thus influencing the behaviour of the two-phase flow, two dimensionless numbers were considered, the Bond number and the Froude number. These numbers describe the relative importance of the three main forces influencing the stratification: the inertial, the gravity and the surface tension forces.

The Bond number is defined as:

$$Bd = \frac{\text{gravity forces}}{\text{surface tension forces}} = \frac{g(\rho_{\text{liq}} - \rho_{\text{vap}})d_{\text{int}}^2}{\sigma} \quad (6)$$

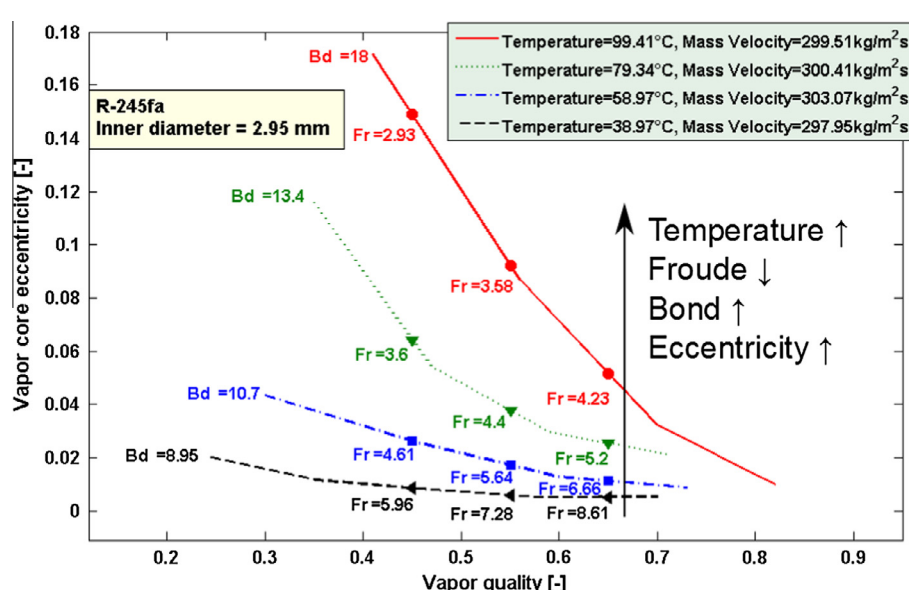


Fig. 19. Influence of saturation temperature on Froude and Bond number and eccentricity at $x = 0.45, 0.55, 0.65$ and $G = 300 \text{ kg/m}^2 \text{ s}$.

where g is the acceleration of gravity, ρ_{liq} and ρ_{vap} are the liquid and vapor densities respectively, d_{int} the internal diameter of the pipe and σ is the surface tension.

The second one is the Froude number, defined as suggested by Cioncolini and Thome [18]. The authors consider the specific kinetic energy of the vapor core divided by a term proportional to the specific gravitational energy of the liquid film in case of complete stratification. The specific kinetic energy of the vapor core has a proportional influence on the shear stress exerted by the gas core onto the liquid film. The resulting Froude number is:

$$\text{Fr} = \frac{\text{inertia forces}}{\text{gravity forces}} = \frac{\frac{xG}{\sqrt{\rho_{\text{vap}}}}}{\sqrt{g(\rho_{\text{liq}} - \rho_{\text{vap}})d_{\text{int}}}} \quad (7)$$

Concerning the influence of these numbers on the stratification, the higher the Bond number, the greater the gravity forces compared to surface tension forces and consequently the greater the stratification. In addition, the higher the Froude number, the greater the inertia forces compared to the gravity forces and the lower the stratification effect. These relationships are summed up in Table 4.

Table 4
Influence of dimensionless numbers on the stratification of the flow.

| | |
|------|------------------|
| Bd ↑ | Stratification ↑ |
| Fr ↑ | Stratification ↓ |

Table 5
Bond number details at $T_{\text{sat}} = 40, 60, 80, 100$ and 115°C .

| $T_{\text{sat}} (\text{°C})$ | Bd (-) | $g(\rho_{\text{liq}} - \rho_{\text{vap}}) \cdot 10^{-2} (\text{N/m})$ | $\sigma \cdot 10^{-3} (\text{N/m})$ | $\rho_{\text{liq}} (\text{kg/m}^3)$ | $\rho_{\text{vap}} (\text{kg/m}^3)$ |
|------------------------------|--------|---|-------------------------------------|-------------------------------------|-------------------------------------|
| 40 | 9.02 | 11.0 | 12 | 1297 | 14.1 |
| 60 | 10.8 | 10.3 | 9.6 | 1237 | 25.6 |
| 80 | 13.5 | 9.62 | 7.1 | 1171 | 43.8 |
| 100 | 18.2 | 8.72 | 4.8 | 1094 | 72.5 |
| 115 | 24.8 | 7.86 | 3.2 | 1026 | 105 |

Therefore, the Bond and Froude numbers were evaluated for each flow condition. A higher saturation temperature provides a higher Bond number and a lower Froude number. This means an increasing importance of the gravity forces compared to the surface tension and inertial forces. The consequence is a higher stratification, as verified in the previous eccentricity analysis. In Fig. 19 is shown the variation of the dimensionless numbers and of the eccentricity with the saturation temperature.

In Table 5, the variation of the Bond number with the temperature is highlighted. Increasing the temperature, the gravitational term decreases, but the surface tension term decreases faster. Hence, Bond number grows with the temperature.

Table 6

Influence of flow conditions on dimensionless numbers and consequence on the stratification of the flow.

| | | |
|---------------------------|-----------|------------------|
| $T_{\text{sat}} \uparrow$ | Bd ↑ Fr ↓ | Stratification ↑ |
| $x \uparrow$ | Bd = Fr ↑ | Stratification ↓ |
| $G \uparrow$ | Bd = Fr ↑ | Stratification ↓ |

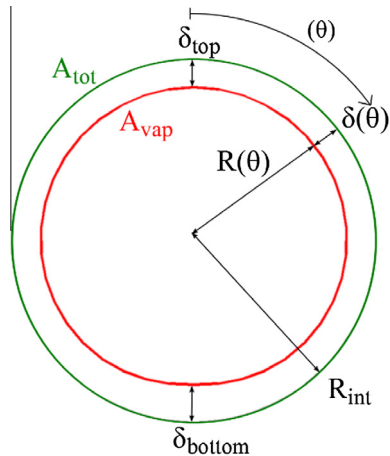


Fig. 21. Schematic of liquid film distribution in the cross-sectional area during annular flow.

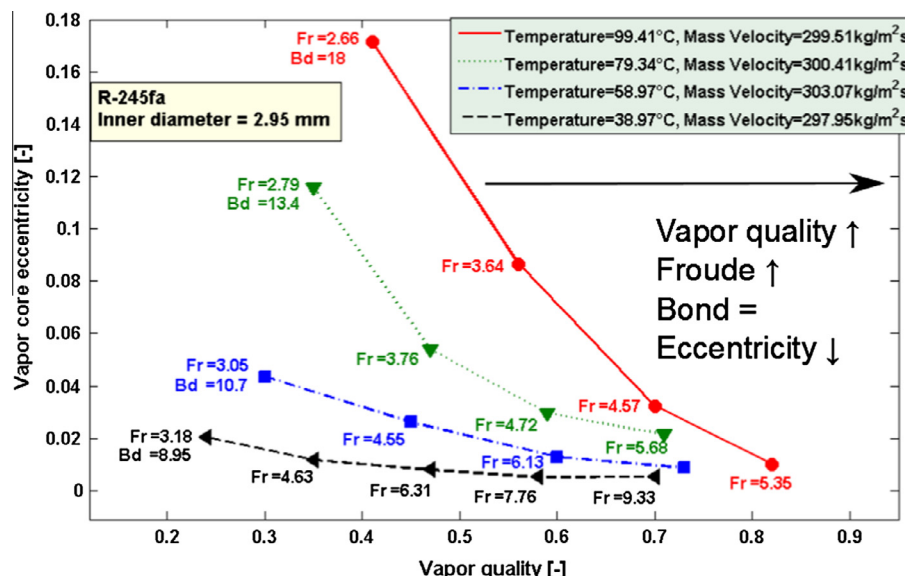


Fig. 20. Influence of vapor quality on Froude and Bond number and eccentricity, for $G = 300 \text{ kg/m}^2 \text{s}$ and $T_{\text{sat}} = 40, 60, 80$ and 100°C .

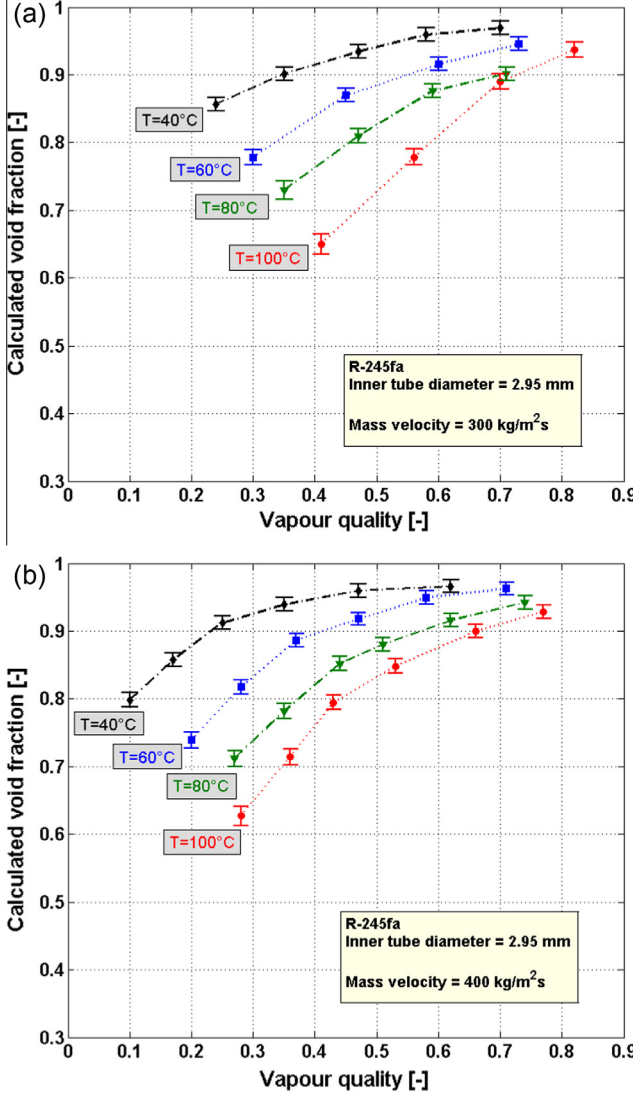


Fig. 22. Calculated cross-sectional void fraction, for $G = 300$ (a) and $400 \text{ kg/m}^2 \text{ s}$ (b).

When increasing the mass velocity or the vapor quality, the Bond number is invariant and the Froude number grows. In fact, the thermodynamic properties of the fluid do not change and consequently the buoyancy and surface tension forces are the same. The only force increasing is the inertial force. This means lower stratification, in agreement with the experimental results. In Fig. 20 is shown the variation of the dimensionless numbers and of the eccentricity with the vapor quality (see Table 6).

4.5. Void fraction measurement

The last step was the cross-sectional void fraction calculation, by knowing the top and bottom film thickness.

The void fraction is given by:

$$\varepsilon = \frac{A_{\text{vap}}}{A_{\text{vap}} + A_{\text{liq}}} = \frac{2 \int_0^\pi \frac{r(\vartheta)^2 \delta \vartheta}{2}}{\pi \cdot R_{\text{int}}^2} = \frac{\int_0^\pi (R_{\text{int}} - \delta(\vartheta))^2 \delta \vartheta}{\pi \cdot R_{\text{int}}^2}$$

$$= \frac{1}{\pi} \int_0^\pi \left(1 - \frac{\delta(\vartheta)}{R_{\text{int}}}\right)^2 d\vartheta \quad (8)$$

where A_{vap} is the area cross-sectional area of the channel occupied by the vapor phase and A_{liq} is that of the liquid phase, R_{int} the internal radius of the pipe, the angle ϑ is measured clockwise from the top of the tube, $r(\vartheta)$ is the local vapor radius and $\delta(\vartheta)$ the local liquid film thickness (see Fig. 21).

The local film thickness distribution was represented by a third-order polynomial interpolation. Its coefficients were found with the following four boundary conditions:

$$\begin{cases} \delta(\vartheta = 0) = \delta_{\text{top}} \\ \delta(\vartheta = \pi) = \delta_{\text{bot}} \\ \frac{\partial \delta}{\partial \vartheta}(\vartheta = 0) = 0 \\ \frac{\partial \delta}{\partial \vartheta}(\vartheta = \pi) = 0 \end{cases} \quad (9)$$

Therefore, the interpolating function is:

$$\varepsilon = \delta_{\text{top}} + \frac{\delta_{\text{bot}} - \delta_{\text{top}}}{\pi^2} \left(3\vartheta^2 - 2\frac{\vartheta^3}{\pi}\right) \quad (10)$$

At each condition, the uncertainty was calculated according to the method presented in [27]:

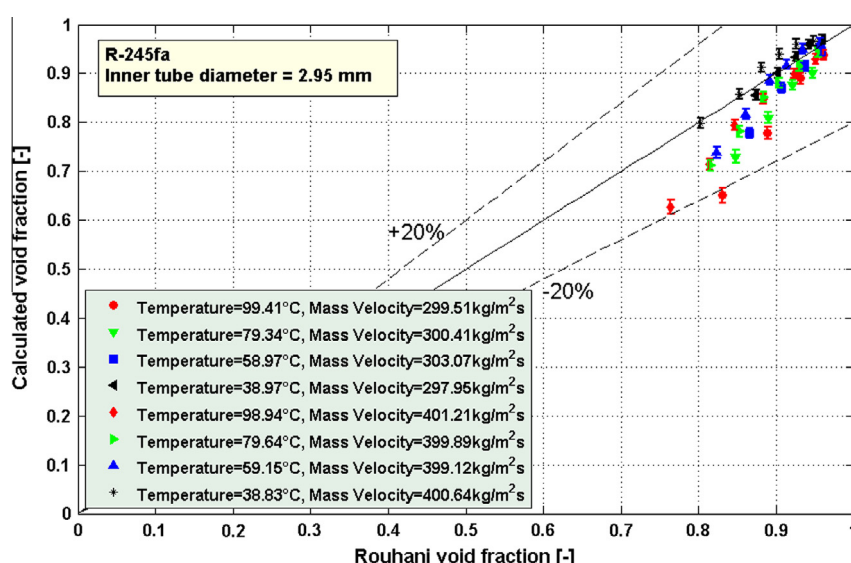


Fig. 23. Void fraction comparison with Rouhani–Axelsson correlation.

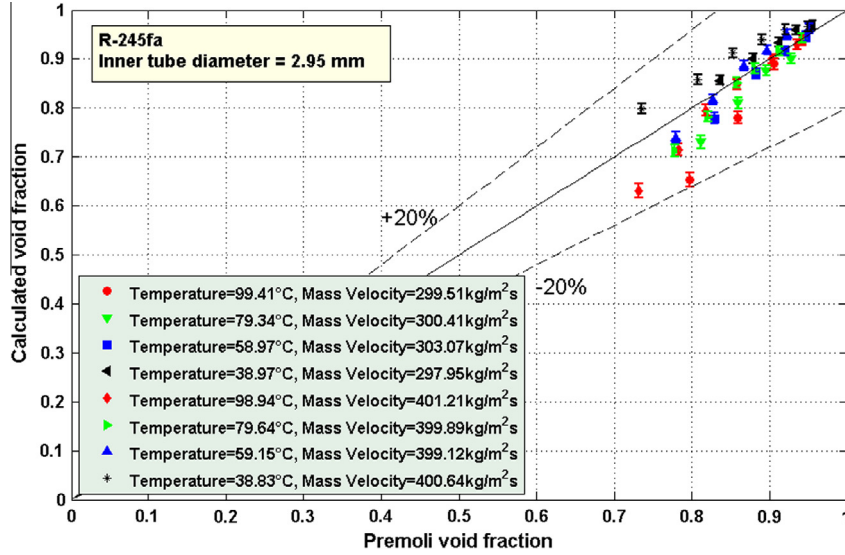


Fig. 24. Void fraction comparison with Premoli correlation.

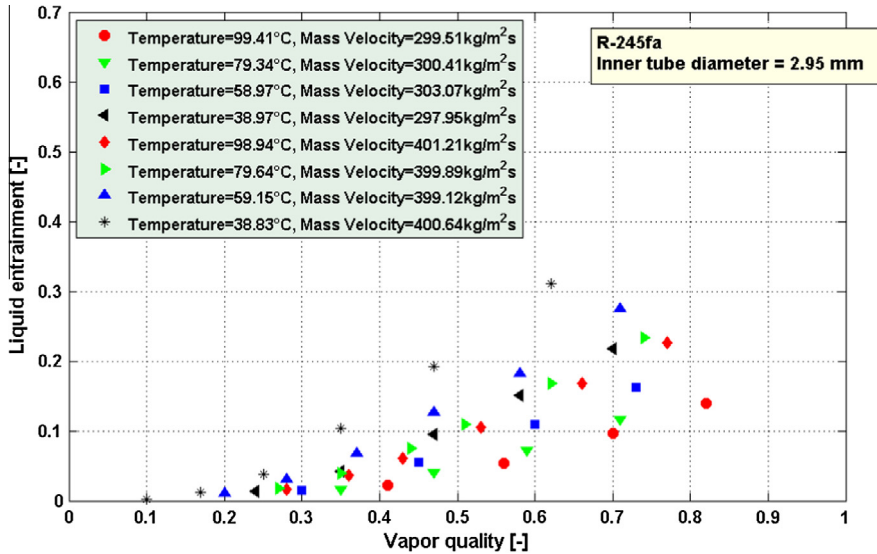


Fig. 25. Liquid entrainment factor for each experimental condition.

$$\delta\epsilon = \sqrt{\left(\frac{\partial\epsilon}{\partial(\delta_{top})}\delta(\delta_{top})\right)^2 + \left(\frac{\partial\epsilon}{\partial(\delta_{bot})}\delta(\delta_{bot})\right)^2 + \left(\frac{\partial\epsilon}{\partial R_{int}}\delta(R_{int})\right)^2} \quad (11)$$

For the whole set of experiments the maximum uncertainty for the void fraction is 1.5%. In Fig. 22, it is shown that the cross-sectional average void fraction grows when decreasing the saturation temperature, which was an expected trend. In fact, when decreasing the temperature, the difference between the liquid and vapor density is larger, so the vapor occupies a major percentage of the section.

Concerning the comparison of the experimental void fraction with quoted void fraction correlations, Woldesemayat and Ghajar [28] show that Steiner version of Rouhani and Axelsson correlation [29] has the best predictive capability for horizontal channels. The authors claimed that another good correlation for horizontal channel is given by Premoli et al. [30] (see Fig. 24).

Fig. 23 shows the comparison with Rouhani and Axelsson correlation. The statistical analysis give MRE and MAE respectively of

4.6% and 5.6%. The standard deviation is 6.9%. The calculated void fraction underestimates the void fraction, especially at higher saturation temperature and lower mass velocity. This behaviour cannot be explained with the liquid entrainment into the vapor core. In facts, for the operating conditions corresponding to the maximum error, the entrainment effect should be negligible, as verified through the Cioncolini and Thome model [31], see results in Fig. 25.

The comparison with Premoli correlation (Fig. 25) shows the points scattered around the bisector, with a good accuracy. The MRE and MAE are respectively 1.6% and 4.1% and the standard deviation is 5.9%.

5. Conclusions

In this paper, an optical method based on an image processing technique allowed to measure accurately the top and bottom film thicknesses for two-phase annular flow in a horizontal minichannel. A high-speed high definition video camera recorded the flow

inside a 2.95 mm inner diameter glass tube. Thus, these frames were processed with an image processing algorithm. By detecting the liquid–vapor and liquid–tube interfaces, the liquid film thickness in terms of pixels was known. After that, the real measurement of the liquid film thickness was obtained through the scale conversion factor (mm/pixel) and by keeping into account the refraction effects inside the tube. For each flow condition, a great number of frames was processed and the average value of the film thickness was evaluated. After the algorithm development, it was possible to get a database of liquid film thickness measurements for different mass velocities, saturation temperatures and vapor qualities. The mean uncertainty on the measurements was about 20%. Information on the stratification were provided with the introduction of the eccentricity of the vapor core. These parameters allowed to state that the stratification of the flow increased with the saturation temperature and decreased with the vapor quality and the mass velocity. Through the dimensionless Bond and Froude numbers, it was possible to explain, physically, the influence of the flow variables on the stratification. Finally, the cross sectional void fraction was evaluated and the results showed a good agreement with Rouhani–Axelsson and Premoli correlations.

Acknowledgments

The experimental work was developed during the stay of Antonio Donniacuo as an Erasmus student at INSA-Lyon, CETHIL, UMR5008. The modeling part was developed also during the stay of Rémi Revellin at Dept. of Industrial Engineering as Visiting Professor with the financial support of the POLIGRID project.

References

- [1] H. Chen, Y. Goswami, E.K. Stefanakos, A review of thermodynamics cycles and working fluids for the conversion of low-grade heat, *Renew. Sust. Energy Rev.* 14 (2010) 3059–3067.
- [2] J. Bao, L. Zhai, A review of working fluid and expander selections for organic Rankine cycle, *Renew. Sust. Energy Rev.* 24 (2013) 325–342.
- [3] F. Cataldo, R. Mastrullo, A.W. Mauro, G.P. Vanoli, Fluid selection of Organic Rankine Cycle for low-temperature waste heat recovery based on thermal optimization, *Energy* 72 (2014) 159–167.
- [4] R. Charnay, R. Revellin, J. Bonjour, Flow boiling characteristics of R-245fa in a minichannel at medium saturation temperatures, *Exp. Therm. Fluid Sci.* 59 (2014) 184–194.
- [5] A. Cioncolini, J.R. Thome, Algebraic turbulence modeling in adiabatic and evaporating annular two-phase flow, *Int. J. Heat Fluid Flow* 32 (2011) 805–817.
- [6] D. Del Col, Flow boiling of halogenated refrigerants at high saturation temperature in a horizontal smooth tube, *Exp. Therm. Fluid Sci.* 34 (2) (2010) 234–245.
- [7] S. Grauso, R. Mastrullo, A.W. Mauro, G.P. Vanoli, Flow boiling of R410A and CO₂ from low to medium reduced pressures in macro channels: experiments and assessment of prediction methods, *Int. Heat Mass Transfer* 56 (2013) 107–118.
- [8] A.W. Mauro, A. Cioncolini, J.R. Thome, R. Mastrullo, Asymmetric annular flow in horizontal circular macro-channels: Basic modeling of liquid film distribution and heat transfer around the tube perimeter in convective boiling, *Int. J. Heat Mass Transfer* 77 (2014) 897–905.
- [9] H. Mori, S. Yoshida, K. Ohishi, Y. Kakimoto, Dryout quality and post-dryout heat transfer coefficient in horizontal evaporator tubes, in: 3rd European Thermal Sciences Conference, Heidelberg, Germany, 2000.
- [10] L. Wojtan, T. Ursenbacher, J.R. Thome, Investigation of flow boiling in horizontal tubes: Part II – Development of a new heat transfer model for stratified-wavy, dryout and mist flow regimes, *Int. J. Heat Mass Transfer* 48 (2005) 2970–2985.
- [11] R. Mastrullo, A.W. Mauro, J.R. Thome, D. Toto, G.P. Vanoli, Flow pattern maps for convective boiling of CO₂ and R410A in a horizontal smooth tube: experiments and new correlations analyzing the effect of the reduced pressure, *Int. J. Heat Mass Transfer* 55 (2012) 1519–1528.
- [12] R. Charnay, R. Revellin, J. Bonjour, Experimental investigation of R-245fa flow boiling in minichannels at high saturation temperatures: flow patterns and flow pattern maps at high saturation temperatures: flow patterns and flow pattern maps, *Int. J. Heat Fluid Flow* 46 (2014) 1–16.
- [13] Y. Luninski, D. Barnea, Y. Taitel, Film thickness in horizontal annular flow, *Can. J. Chem. Eng.* 61 (1983) 621–626.
- [14] J.E. Laurinat, T.J. Hanratty, J.C. Dallman, Pressure drop and film height measurements for annular gas–liquid flow, *Int. J. Multiphase Flow* 10 (3) (1984) 341–356.
- [15] T. Fukano, A. Ousaka, Prediction of the circumferential distribution of film thickness in horizontal and near-horizontal gas–liquid annular flows, *Int. J. Multiphase Flow* 15 (3) (1989) 403–419.
- [16] E.T. Hurlburt, T.A. Newell, Optical measurement of liquid film thickness and wave velocity in liquid film flows, *Exp. Fluids* 21 (1996) 357–362.
- [17] T.A. Shedd, T.A. Newell, Automated optical liquid film thickness measurement method, *Rev. Sci. Instrum.* 69 (1998) 4205–4213.
- [18] A. Cioncolini, J.R. Thome, Liquid film circumferential asymmetry prediction in horizontal annular two-phase flow, *Int. J. Multiphase Flow* 51 (2013) 44–54.
- [19] R. Charnay, R. Revellin, J. Bonjour, Flow pattern characterization for R-245fa in minichannels: optical measurement technique and experimental results, *Int. J. Multiphase Flow* 57 (2013) 169–181.
- [20] C.B. Tibiriçá, F.J. do Nascimento, G. Ribatski, Film thickness measurement techniques applied to micro-scale two-phase flow systems, *Exp. Therm. Fluid Sci.* 34 (2010) 463–473.
- [21] T. Takamasa, T. Hazuku, Measuring interfacial waves on film flowing down a vertical plate wall in the entry region using laser focus displacement meters, *Int. J. Heat Mass Transfer* 43 (2000) 2807–2819.
- [22] T. Takamasa, K. Kobayashi, Measuring interfacial waves on film flowing down tube inner wall using laser focus displacement meter, *Int. J. Multiphase Flow* 26 (2000) 1493–1507.
- [23] C.L. Ong, J.R. Thome, Macro-to-microchannel transition in two-phase flow: Part 1 – Two-phase flow patterns and film thickness measurements, *Exp. Therm. Fluid Sci.* 35 (2011) 37–47.
- [24] A. Kawahara, P.M.-Y. Chung, M. Kawaji, Investigation of two-phase flow pattern, void fraction and pressure drop in a microchannel, *Int. J. Multiphase Flow* 28 (2002) 1411–1435.
- [25] X. Fu, P. Zhang, H. Hu, C.J. Huang, Y. Huang, R.Z. Wang, 3D visualization of two-phase flow in the micro-tube by a simple but effective method, *J. Micromech. Microeng.* 19 (2009) 085005. 11pp.
- [26] J.W. Schmidt, E. Carrillo-Nava, M.R. Moldover, Partially halogenated hydrocarbons CHFCl-CF₃, CF₃-CH₃, CF₃-CHF-CHF₂, CF₃-CH₂-CF₃, CHF₂-CF₂-CH₂F, CF₃-CH₂-CHF₂, CF₃-O-CHF₂: critical temperature, refractive indices, surface tension and estimates of liquid, vapor and critical densities, *Fluid Phase Equilib.* 122 (1996) 187–206.
- [27] J.R. Taylor, *An Introduction to Error Analysis: The Study of Uncertainties in Physical Measurements*, second ed., University Science Books, 1997.
- [28] M.A. Woldesemayat, A.J. Ghajar, Comparison of void fraction correlations for different flow patterns in horizontal and upward inclined pipes, *Int. J. Multiphase Flow* 33 (2007) 347–370.
- [29] D. Steiner, *VDI-Wärmeatlas (VDI Heat Atlas)*, Springer, 1993 (chapter Hbb).
- [30] A. Premoli, D. Di Francesco, A. Prima, An empirical correlation for evaluating two-phase mixture density under adiabatic conditions, in: European Two-Phase Flow Group Meeting, Milan, Italy, 1970.
- [31] A. Cioncolini, J.R. Thome, Entrained liquid fraction prediction in adiabatic and evaporating annular two-phase flow, *Nucl. Eng. Des.* 243 (2012) 200–213.